Proton and Electron Conductivity in Hydrous Ruthenium Oxides Evaluated by Electrochemical Impedance Spectroscopy: The Origin of Large Capacitance

Wataru Sugimoto,* Hideki Iwata, Katsunori Yokoshima, Yasushi Murakami, and Yoshio Takasu

Department of Fine Materials Engineering, Faculty of Textile Science and Technology, Shinshu University, 3-15-1 Tokida, Ueda 386-8567, Japan

Electrochemical impedance spectroscopy was conducted on a series of hydrous ruthenium oxides, $RuO_2 \cdot xH_2O$, ($x = 0.5, 0.3, 0$) and a layered ruthenic acid hydrate ($H_{0.2}RuO_{2.1} \cdot nH_2O$) in order to evaluate their protonic and electronic conduction. The capacitor response frequency was observed at lower frequency for $RuO_2 \cdot xH_2O$ with higher water content, which was suggested to be due to electrolyte exhaustion within the film and/or utilization of hydrated interparticle micropores that have high ionic resistance. Analysis of the impedance data indicated that the charge-transfer resistance through the film is not significantly affected by the water content in $RuO_2 \cdot xH_2O$, and the capacitor frequency response is dominated by the protonic conduction. The capacitor response frequency of layered $H_{0.2}RuO_{2.1} \cdot nH_2O$ was comparable to $RuO_2 \cdot 0.5H_2O$. The high specific capacitance at low frequency for layered $H_{0.2}RuO_{2.1} \cdot nH_2O$ is attributed to the utilization of the expandable hydrous interlayer, which accounts for the ionic conduction. The present results demonstrate the importance of hydrous regions (either interparticle or interlayer) to allow appreciable protonic conduction for high energy and high power electrochemical capacitors.

1. Introduction

Electrochemical capacitors (also known as supercapacitors or ultracapacitors) have attracted increased interest due to their high power density and long cycle life compared to batteries, and high energy density compared to conventional capacitors.[1−5] In particular, electrochemical capacitors based on ruthenium oxides (so-called pseudo-capacitors or redox-capacitors) can provide higher energy density than conventional electric double-layer capacitors based on carbon.[1,5−11] RuO_2-based materials have been studied as chlorine and oxygen evolving anodes, and hydrogen evolving cathodes. Much of the early work on RuO_2-based electrodes was focused on the electrocatalytic properties of thermally prepared porous electrodes known as DSA [see refs 12−15 for comprehensive reviews]. Trasatti and Buzzanca[16] were the first to notice that the 'rectangular' shaped cyclic voltammogram of a RuO_2 film resembled that of the carbon-based electric double layer capacitors. Since then, much effort has been devoted to enhancing the capacitance as well as the fundamental understanding of the mechanism of the pseudocapacitance.

The study by Zheng and Jow on hydrous ruthenium oxide ($RuO_2 \cdot xH_2O$) prepared by a sol−gel procedure was a major breakthrough in terms of mass specific capacitance;[17,18] they were able to double the capacitance from the highest reported value at that time. The specific capacitance for hydrous ruthenium oxide ($RuO_2 \cdot xH_2O$) ranges from 600 to 800 F g^{-1} depending on the preparation procedure and measurement conditions,[17−21] which is 3 to 5 times higher than that of electric double-layer capacitors or anhydrous RuO_2. Thus, $RuO_2 \cdot xH_2O$ can be taken as one of the most promising material for high energy density electrochemical capacitors. The higher energy density compared to anhydrous RuO_2 has been attributed to the mixed protonic−electronic conduction of $RuO_2 \cdot xH_2O$. It has been proposed that the hydrous regions within the nanoparticles allows facile proton permeation into the bulk material for efficient charge storage while the interconnected ruthenium oxide region accounts for the electronic conduction.[18] Using solid state ^1H NMR, Fu et al. has revealed that the specific capacitance is strongly correlated with the proton mobility.[19d] An optimum mixed percolation conduction mechanism where separate percolation paths provide protonic and electronic conduction has also been proposed.[20d]

Although $RuO_2 \cdot xH_2O$ offers higher energy density compared to anhydrous RuO_2, such high energy density generally cannot be obtained at high current density. Hence, the improvement in the power density of $RuO_2 \cdot xH_2O$ with relatively high water content is one of the challenges. Considerable amount of effort has been devoted to the hybridization of $RuO_2 \cdot xH_2O$ with carbon[19c,22] or conducting polymers.[23] The hybridization has shown to be effective for increasing the high rate characteristics with the sacrifice of the overall mass-specific capacitance (energy density). The positive effect of the physical mixing of carbon has been discussed based on an "electrolyte reservoir" mechanism.[19c] The low electronic conductivity at high water content due to lack of electronic conducting pathways[20d] may also contribute to the lower power density.

A different type of hydrous ruthenium oxide, layered ruthenic acid hydrate ($H_{0.2}RuO_{2.1} \cdot nH_2O$), is also a promising electrode material with mixed protonic−electronic conduction.[24,25] Unlike $RuO_2 \cdot xH_2O$, layered $H_{0.2}RuO_{2.1} \cdot nH_2O$ is a crystalline oxide with a lamellar structure, and the electronic conduction is provided via the crystalline ruthenium oxide nanosheets that is interleaved in a nanometer scale with a hydrous layer accounting for the protonic conduction. We have shown that layered $H_{0.2}RuO_{2.1} \cdot nH_2O$ can deliver specific capacitance up to 390 F g^{-1}.

* To whom correspondence should be addressed. E-mail: wsugi@shinshu-u.ac.jp.

Impedance of Mixed Conducting Hydrous Ruthenates

J. Phys. Chem. B, Vol. 109, No. 15, 2005 **7331**

Furthermore, ruthenium oxide nanosheets derived from $H_{0.2}$-$RuO_{2.1} \cdot nH_2O$ by chemical exfoliation (de-lamination) exhibited specific capacitance up to 700 F g^{-1}, which is comparable with conventional $RuO_2 \cdot xH_2O$.

In a recent study using dc resistivity measurements, we reported that the layered ruthenates possess metallic conductivity with room-temperature resistivity in the order of mΩ cm,[26] comparable to that of $RuO_2 \cdot xH_2O$.[18] To further understand the properties and differences in the fundamental capacitive behavior of $RuO_2 \cdot xH_2O$ and layered $H_{0.2}RuO_{2.1} \cdot nH_2O$, it is important that the frequency response and protonic−electronic conduction of these materials are comprehended.

Electrochemical impedance spectroscopy is a useful method to obtain information on the protonic conduction of hydrous materials. Impedance analysis has been utilized to understand the resistance and specific capacitance of single-cell[27] and half-cell electrodes[28] for electrochemical capacitor application. However, discussion so far has been confined to the assessment of the specific capacitance or change in the electrolyte resistance, and the effect of the water content on the frequency response has not been considered. In this study, we have evaluated the capacitor frequency response of $RuO_2 \cdot xH_2O$ as a function of the water content as well as layered $H_{0.2}RuO_{2.1} \cdot nH_2O$ by electrochemical impedance spectroscopy and discuss the electronic and protonic conduction of these materials.

2. Experimental Section

2.1. Materials. Commercially available hydrous ruthenium oxide (Johnson Matthey Co. Stock #43403) was heat treated at 450, 300, or 200 °C for 24 h in air to prepare hydrous ruthenium oxide with a range of water contents. The water content of the products after the heat treatment was analyzed by thermoanalysis (TG-DTA; Rigaku TAS-200). Layered ruthenic acid hydrate was prepared as reported earlier.[24−26] X-ray diffraction (XRD) (Rigaku RINT 2550H/PC; monochromated Cu−Kα radiation) was utilized to study the structure of the products.

2.2. Cyclic Voltammetry. A beaker-type electrochemical cell was used for the electrochemical measurements. The cell was equipped with a working electrode, a platinum mesh counter electrode, and an Ag/AgCl reference electrode. Electrode potentials will be referred to the reversible hydrogen electrode (RHE) potential scale. A Luggin capillary faced the working electrode at a distance of 2 mm. The working electrodes were prepared by the thin film electrode method.[29,30] This method allows the straightforward evaluation of the intrinsic electrochemical capacitor properties of nanoparticulate oxides.[31] Briefly, 20 mg of nanoparticulate $RuO_2 \cdot xH_2O$ or layered $H_{0.2}$-$RuO_{2.1} \cdot nH_2O$ was dispersed in 10 cm^3 distilled water and was subject to ultrasonification for 30 min. A total of 20 mm^3 of the magnetically stirred dispersion was then pipetted onto a mirror-polished Glassy Carbon rod (5 mm diameter). After drying, 20 mm^3 of a 1 wt % Nafion ionomer solution was then dropped onto the electrode surface to immobilize the active material. All electrochemical studies were conducted at 25 °C in 0.5 M H_2SO_4. Cyclic voltammetry was conducted between 0.2 and 1.2 V vs RHE at scan rates of 500 to 2 mV s^{-1} (Hokuto Denko HZ-3000). The specific capacitance was calculated by averaging the anodic and cathodic charge after at least 500 break-in cycles at 50 mV s^{-1}. The specific capacitance is reported in unit of Farads per mass of RuO_2 (F (g-RuO_2)$^{-1}$) to allow uncomplicated comparison between different materials.

2.3. Electrochemical Impedance Spectroscopy. Electrochemical impedance spectroscopy (Solartron 1287 Electrochemical Interface, 1255B Frequency Response Analyzer) was
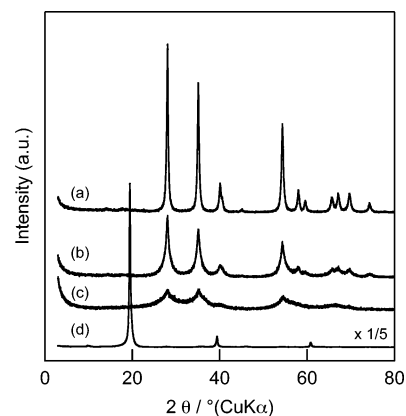
Figure 1. XRD patterns of $RuO_2 \cdot xH_2O$ with $x =$ (a) 0, (b) 0.3, (c) 0.5, and (d) layered $H_{0.2}RuO_{2.1}$.

carried out in the same type of beaker-type electrochemical cell as that for cyclic voltammetry, except that a Pt pseudo-reference electrode was used instead of an Ag/AgCl reference electrode in order to obtain reliable impedance data at high frequency. Impedance measurements were conducted after the cyclic voltammetry studies in a constant voltage mode (0.2, 0.4, 0.6, 0.8, 1.0, 1.2 V vs RHE) by sweeping frequencies from 50 kHz to 10 mHz at an amplitude of 5 mV. The impedance data are normalized to the geometric surface area of the Glassy Carbon electrode (0.196 cm^2).

3. Results

3.1. Structural Characterization of $RuO_2 \cdot xH_2O$ and Layered $H_{0.2}RuO_{2.1}$. The water content x in $RuO_2 \cdot xH_2O$ for the products treated at 450, 300, and 200 °C was 0, 0.3, and 0.5, as determined from TG-DTA. Diffraction peaks ascribable to rutile-type RuO_2 were observed in the XRD patterns (Figure 1a−c) with the peak intensity decreasing and peak width widening with increasing water content. The widening of the peak width can be attributed to the decrease in the primary particle size with decreasing temperature of heat treatment, and the decrease in peak intensity suggests a decrease in the amount of crystalline RuO_2 and/or inferior crystallinity. The XRD pattern for $H_{0.2}RuO_{2.1}$ is shown in Figure 1d. The XRD pattern revealed a layered structure with interlayer spacing of 0.457 nm, in agreement with our previous study.[24]

3.2. Electrochemical Properties of Anhydrous RuO_2. Cyclic voltammograms at scan rates ranging from 500 to 2 mV s^{-1} for anhydrous RuO_2 are shown in Figure 2a. The cyclic voltammograms can be divided into three types of reactions, namely the electric double-layer charging, the redox related charging at ∼0.6 and ∼0.8 V vs RHE due to electrosorption of ions on the surface of the oxide, and proton diffusion into defect sites, interstitial sites, and/or grain boundaries below 0.4 V vs RHE.[31,32] The specific capacitance at various scan rates acquired from cyclic voltammetry are summarized in Table 1.

The complex-plane impedance and admittance plots (Nyquist plots) at different potentials for anhydrous RuO_2 are given in Figure 3a,b. The complex-plane impedance plots exhibit a line with a slope close to 90° along the imaginary axis (Z'') when $E \geq$ 0.6 V vs RHE, characteristic of an ideally polarizable electrode. A slight deviation from the straight line along the imaginary axis (Z'') is apparent for $E \leq$ 0.4 V vs RHE, suggestive of a nonideally polarizable electrode. This is in correspondence to the scan rate dependent current observed below 0.4 V vs RHE in the cyclic voltammograms (Figure 2a). The deviation from the 90° slope along the imaginary axis when

7332 *J. Phys. Chem. B, Vol. 109, No. 15, 2005*

Sugimoto et al.
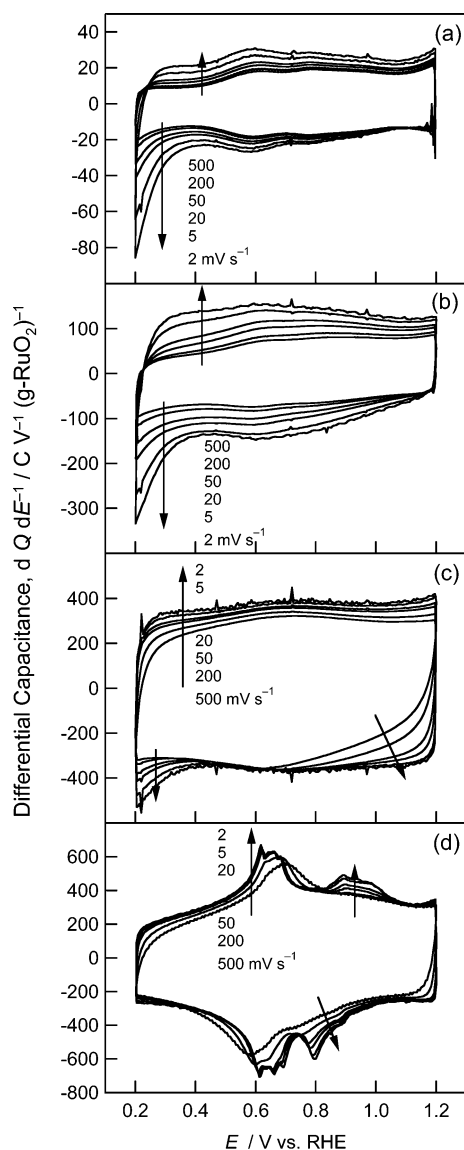
Figure 2. Cyclic voltammograms of $RuO_2 \cdot xH_2O$ with x = (a) 0, (b) 0.3, (c) 0.5, and (d) layered $H_{0.2}RuO_{2.1} \cdot nH_2O$ at 2, 5, 20, 50, 200, 500 mV s^{-1}. Mass of material: 40 μg. Electrolyte: 0.5 M H_2SO_4 (25 °C).

TABLE 1: Specific Capacitance Obtained by Cyclic Voltammetry at Various Scan Rates for $RuO_2 \cdot xH_2O$ and Layered $H_{0.2}RuO_{2.1} \cdot nH_2O$

scan rate, mV s^{-1}	specific capacitance/F (g-RuO_2)$^{-1}$			
	RuO_2	$RuO_2 \cdot 0.3H_2O$	$RuO_2 \cdot 0.5H_2O$	$H_{0.2}RuO_{2.1} \cdot nH_2O$
2	24	124	342	381
5	22	112	331	376
20	19	93	316	367
50	18	82	304	358
200	16	68	280	342
500	15	61	256	325

$E \leq 0.4$ V vs RHE is attributed to the redox-related capacitance due to proton diffusion.

The frequency dependence of the magnitude $|Z|$, the phase angle ϕ, and the capacitance C (Bode plots) at different potentials are shown in Figure 3c–e. The Bode plots can be separated into three regions, namely the high frequency, medium frequency, and low-frequency regions. At the high-frequency regions, $|Z|$ is weakly dependent on f, and the phase angle and capacitance are near zero. The lower limit of the high-frequency region is characterized by the knee frequency in the complex-plane plots (shown in Figure 3b) and is 1.6–2.5 kHz. The low-

frequency region is defined as the region where the f–$|Z|$ plot shows a slope close to -1, and $-90° < \phi < -45°$ in the f–ϕ plot. The near -1 slope shows that this region is typical of capacitive behavior. The frequency where $\phi = -45°$ ($f_{\phi=-45}$) can be recognized as the frequency response to the ideally capacitive behavior (capacitor response frequency). The $f_{\phi=-45}$ values ranged from 50 to 130 Hz, giving the response time of the capacitor as 20–10 ms. The f–C plot shows that the capacitance levels-off at frequencies below the capacitor response frequency when $E \geq 0.6$ V vs RHE. The capacitance continuously increases for $E \leq 0.4$ V vs RHE, due to the contribution of proton diffusion into grain boundaries. The maximum specific capacitance was calculated from the low-frequency data using the equation $Z'' = (2\pi fC)^{-1}$ where Z'' is the imaginary part of the impedance, f is the frequency, and C is the capacitance. The specific capacitance at different potentials calculated from the Z'' value at the lowest frequency ($f = 10$ mHz) is summarized in Table 2. The potential dependency of the specific capacitance obtained from the electrochemical impedance spectroscopy is in good agreement with that obtained from cyclic voltammetry (Figure 2a and Table 1).
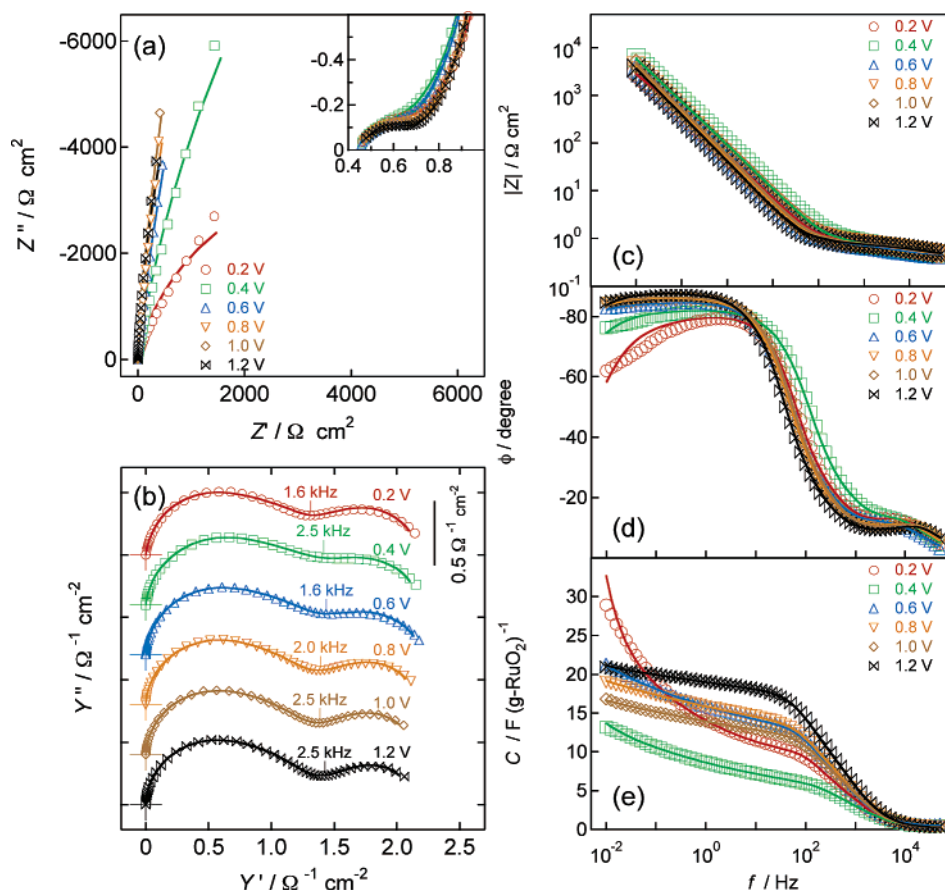
3.3. Electrochemical Properties of $RuO_2 \cdot 0.3H_2O$. Cyclic voltammograms at various scan rates for $RuO_2 \cdot 0.3H_2O$ are shown in Figure 2b. The shape of the cyclic voltammograms of $RuO_2 \cdot 0.3H_2O$ are similar to anhydrous RuO_2, showing the redox related charge near 0.6 and 0.8 V vs RHE and a large cathodic current below 0.4 V vs RHE. The specific capacitance is about 5 times higher than anhydrous RuO_2. (Table 1).

The Nyquist and Bode plots at different potentials for $RuO_2 \cdot 0.3H_2O$ are given in Figure 4. The impedance behavior of $RuO_2 \cdot 0.3H_2O$ is analogous to that of anhydrous RuO_2 (Figure 3), indicating that the intrinsic charge storage mechanism is qualitatively similar. Quantitatively, $RuO_2 \cdot 0.3H_2O$ is quite different from anhydrous RuO_2. First, the deviation from the $\sim 90°$ angle along the imaginary axis (Z'') for $E = 0.2$ V vs RHE is not as prominent for $RuO_2 \cdot 0.3H_2O$. This is in correspondence to the cyclic voltammograms showing that the cathodic current is not as obvious. Second, the redox-related charge at ~ 0.6 and ~ 0.8 V vs RHE due to electrosorption of ions on the surface of the oxide are enhanced. Third, the capacitor response frequencies $f_{\phi=-45}$ were shifted to lower frequency.

The Bode plots of $RuO_2 \cdot 0.3H_2O$ shows that the high frequency characteristic is quantitatively the same. The knee frequency is observed at similar frequency as anhydrous RuO_2 at 2.0–3.2 kHz. This suggests that despite the difference in the capacitor response frequency $f_{\phi=-45}$, the charge-transfer resistance of $RuO_2 \cdot 0.3H_2O$ and anhydrous RuO_2 is comparable. The capacitor response frequency $f_{\phi=-45}$ ranged from 15 to 30 Hz, which is relatively lower than anhydrous RuO_2 ($f_{\phi=-45} = 50$–130 Hz). The response time of the capacitor is approximately 65–30 ms, a few times slower than anhydrous RuO_2 (20–10 ms). The f–C plot indicates that the capacitance at low frequencies below the capacitor response frequency $f_{\phi=-45}$ does not completely level off as in the case of anhydrous RuO_2. This is correlated to the larger contribution from the redox-related charge that is scan-rate dependent observed in the cyclic voltammograms in the case of $RuO_2 \cdot 0.3H_2O$ (Figure 2a and 2b). The potential dependency of the specific capacitance obtained from the electrochemical impedance spectroscopy is in good agreement with that obtained from cyclic voltammetry (Figure 2b and Tables 1, 2).

3.4. Electrochemical Properties of $RuO_2 \cdot 0.5H_2O$. Cyclic voltammograms at various scan rates for $RuO_2 \cdot 0.5H_2O$ are

Impedance of Mixed Conducting Hydrous Ruthenates

J. Phys. Chem. B, Vol. 109, No. 15, 2005 **7333**

Figure 3. The (a) complex-plane impedance and (b) admittance plots at various electrode potentials for anhydrous RuO_2. The characteristic knee frequency is shown in b. Frequency dependence of the (c) magnitude $|Z|$, (d) phase angle ϕ, and (e) specific capacitance C. Mass of material: 40 μg. Electrolyte: 0.5 M H_2SO_4 (25 °C). The solid lines represent the fitted data to the equivalent circuit Figure 7.

TABLE 2: Specific Capacitance Obtained from Electrochemical Impedance Spectroscopy at Various Potentials for $RuO_2 \cdot xH_2O$ and Layered $H_{0.2}RuO_{2.1} \cdot nH_2O$

potential, V vs RHE	specific capacitance/F (g-RuO_2)$^{-1}$			
	RuO_2	$RuO_2 \cdot 0.3H_2O$	$RuO_2 \cdot 0.5H_2O$	$H_{0.2}RuO_{2.1} \cdot nH_2O$
0.2	31	140	305	201
0.4	13	86	296	276
0.6	20	101	328	597
0.8	19	97	351	382
1.0	16	81	345	291
1.2	22	79	371	318

shown in Figure 2c. The redox-related charge at 0.6 and 0.8 V vs RHE and the cathodic current below 0.4 V vs RHE are obscured compared to $RuO_2 \cdot 0.3H_2O$ and anhydrous RuO_2, leading to featureless and rectangular shaped voltammograms. The lack of the large cathodic current below 0.4 V vs RHE for the more hydrated systems can be attributed to the fact that most or all grain boundaries are hydrated; thus, there is no charge storage by proton injection into such regions. The specific capacitance is about 3 times higher than $RuO_2 \cdot 0.3H_2O$ and 15 times higher than anhydrous RuO_2 (Table 1).

The Nyquist and Bode plots at the respective potentials for $RuO_2 \cdot 0.5H_2O$ are given in Figure 5. The deviation from the ∼90° angle along the imaginary axis (Z'') for $E = 0.2$ V vs RHE is not observed in $RuO_2 \cdot 0.5H_2O$ corresponding with the featureless cyclic voltammograms. The capacitor response frequency $f_{\phi=-45}$ is shifted further to lower frequency.

The knee frequency for $RuO_2 \cdot 0.5H_2O$ is the same range as $RuO_2 \cdot 0.3H_2O$ and anhydrous RuO_2 at 0.6−3.2 kHz, indicating that the charge-transfer resistance is independent of the water content. The capacitor response frequency $f_{\phi=-45}$ ranged from

2 to 4 Hz, which is 1 to 2 orders lower than anhydrous RuO_2 ($f_{\phi=-45} = 50−130$ Hz) and $RuO_2 \cdot 0.3H_2O$ ($f_{\phi=-45} = 15−30$ Hz). The response time of the capacitor is considerably slower compared to anhydrous RuO_2 (20−10 ms) at 500−250 ms.

**3.5. Electrochemical Properties of Layered $H_{0.2}RuO_{2.1} \cdot nH_2O$.** Cyclic voltammograms at various scan rates for layered $H_{0.2}RuO_{2.1} \cdot nH_2O$[33] are shown in Figure 2d. The redox-related charge at 0.6 and 0.8 V vs RHE is significantly higher than $RuO_2 \cdot xH_2O$. The larger contribution from these redox-related charges is attributed to the ionic transport into the interlayer, as will be discussed in the next section. The specific capacitance is close to that of $RuO_2 \cdot 0.5H_2O$ (Table 1).

Despite the crystalline nature of layered $H_{0.2}RuO_{2.1} \cdot nH_2O$, its impedance behavior (Figure 6) is similar to $RuO_2 \cdot 0.5H_2O$, except that the $f-C$ plots are strongly dependent on the potential. This is in correspondence to the nonrectangular shape of the cyclic voltammograms.

The knee frequency for layered $H_{0.2}RuO_{2.1} \cdot nH_2O$ is observed at 0.3−0.6 kHz, slightly lower compared to $RuO_2 \cdot xH_2O$ (0.6−3.2 kHz). The capacitor response frequency $f_{\phi=-45}$ ranged from 2 to 5 Hz, giving the response time of the capacitor at 500−200 ms, similar to the values for $RuO_2 \cdot 0.5H_2O$. Despite the crystalline nature of layered $H_{0.2}RuO_{2.1} \cdot nH_2O$, the response time of the capacitor is considerably slower compared to anhydrous RuO_2 (20−10 ms).

4. Disucussion

The pseudo-capacitance of oxide electrodes in acidic electrolytes should involve many processes, such as the electric double-layer charging at the outer Helmholtz plane, polarization
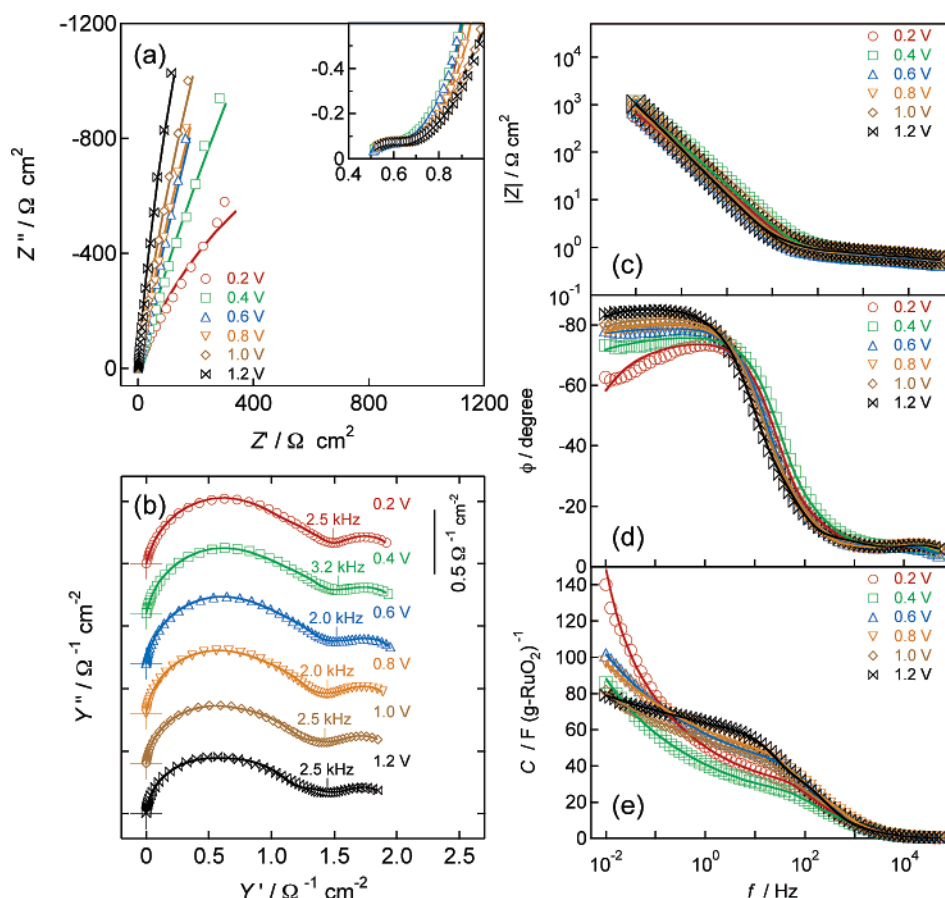
Figure 4. The (a) complex-plane impedance and (b) admittance plots at various electrode potentials for RuO$_2$·0.3H$_2$O. The characteristic knee frequency is shown in b. Frequency dependence of the (c) magnitude $|Z|$, (d) phase angle ϕ, and (e) specific capacitance C. Mass of material: 40 μg. Electrolyte: 0.5 M H$_2$SO$_4$ (25 °C). The solid lines represent the fitted data to the equivalent circuit Figure 7.

of water at the electrode/electrolyte interface, electrosorption of ions at the electrode surface, and sometimes proton diffusion into defect sites, interstitial sites, and/or grain boundaries. In the case of porous and hydrous oxides as those used in this study, nonhomogeneity will also be introduced, further complicating the impedance spectra. The charge storage in layered H$_{0.2}$RuO$_{2.1}$·nH$_2$O will be even more complicated due to the involvement of the interlayer. The impedance data was analyzed assuming three major reactions at high, medium, and low-frequency attempting to keep the model circuit as simple as possible. At high frequency ($f \geq$ 2.5 kHz), mass transfer can be neglected and the charge-transfer process at the outermost surface of the electrode in contact with the electrolyte will be dominant. The medium-frequency region will be diffusion controlled, and the distributed capacitance and resistance within the film will dominate the impedance. At the low-frequency range ($f \leq f_{\phi=-45}$), nonhomogeneous diffusion in the less-accessible sites or leakage current may govern the impedance.

The high frequency data shows that the knee frequency separating the high and medium frequency was insignificantly dependent on the water content or the structure at $f = 0.3-3.2$ kHz. Therefore, the electronic conductivity through the film is not severely affected by these parameters and the change in the electronic conductivity can be considered as a negligible contribution to the capacitor frequency response.

Figure 7 shows the equivalent circuit employed to fit the experimental impedance data. The high and medium-frequency data were fitted with a Randles-type circuit $R_s(C(R_1 Z_W))$, where R_s is the solution resistance, C is the capacitance at high frequency of the outermost surface of the film, and Z_W is the

finite length Warburg impedance element. The impedance of the capacitance can be expressed as

$$Z_c = \frac{1}{i\omega C} \tag{1}$$

where $i = \sqrt{-1}$, ω is the angular frequency, and C is the capacitance. The Warburg impedance Z_W can be expressed as

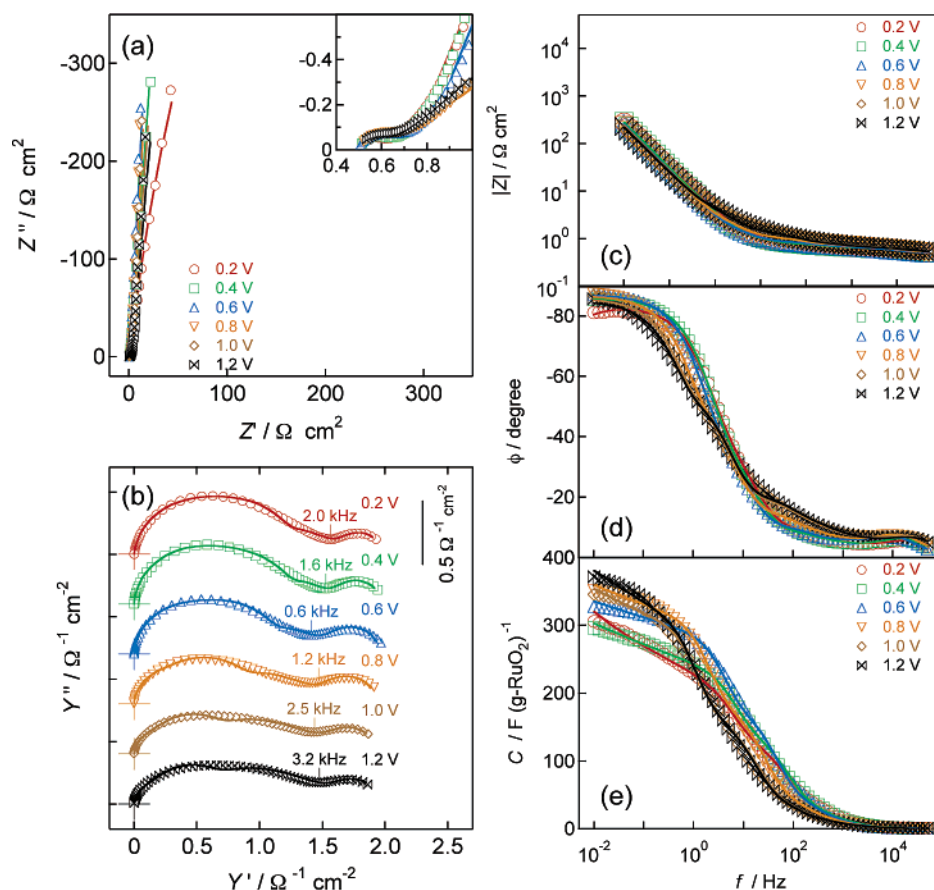$$Z_W = \frac{R_W \coth[(iT_W\omega)^{\alpha_W}]}{(iT_W\omega)^{\alpha_W}} \tag{2}$$

where R_W is the limiting diffusion resistance, T_W is expressed as $T_W = L^2/D$, where L is the effective diffusion length and D is the effective diffusion coefficient, and α_W is a fractional exponent between 0 and 1.

The finite length Warburg impedance element was used to describe the highly distributed capacitance within the hydrous network of the film. It is similar to a finite length transmission line with capacitive termination. Such an element has often been used to describe the finite length ion transport through thin film oxides and polymers.[34] An additional $R_2(CPE\ R_3)$ circuit was connected in parallel to account for the low-frequency Faradaic impedance. The impedance of the CPE can be expressed as

$$Z_{CPE} = \frac{1}{T_{CPE}(i\omega)^{\alpha_W}} \tag{3}$$

where, T_{CPE} is the capacitance when $\alpha_{CPE} = 1$, and α_{CPE} is the constant phase exponent ($0 \leq \alpha_{CPE} \leq 1$). A CPE was used

Impedance of Mixed Conducting Hydrous Ruthenates

J. Phys. Chem. B, Vol. 109, No. 15, 2005 **7335**

Figure 5. The (a) complex-plane impedance and (b) admittance plots at various electrode potentials for $RuO_2 \cdot 0.5H_2O$. The characteristic knee frequency is shown in b. Frequency dependence of the (c) magnitude $|Z|$, (d) phase angle ϕ, and (e) specific capacitance C. Mass of material: 40 μg. Electrolyte: 0.5 M H_2SO_4 (25 °C). The solid lines represent the fitted data to the equivalent circuit Figure 7.

instead of a capacitor to account for the inhomogeneity of the film. Overall, the model circuit comprises of 7 elements (Figure 7) and can be written as:

$$Z_{total} = R_1 + (Z_c^{-1} + (R_1 + Z_w)^{-1} + \\ (R_2 + (R_3^{-1} + Z_{CPE}^{-1})^{-1})^{-1})^{-1} \quad (4)$$

The fitted data (solid lines in Figures 3−6) agrees well with the experimental data. Selected parameters are available as supplementary data (Table S1). The C values were ~10 μF cm^{-2}(geometric), consistent with the capacitance of the outermost surface.

The value of T_W decreased drastically with decreasing water content in $RuO_2 \cdot xH_2O$, indicating either a decrease in the diffusion length L or an increase in the effective diffusion coefficient D. Recent solid-state ^{1}H NMR studies on the proton mobility of $RuO_2 \cdot xH_2O$ by Fu et al. has shown that the proton activation energy is higher for a less hydrated system.[19d] Thus, an increase in the effective diffusion coefficient D with decreasing water content is unreasonable. A more plausible explanation for the decrease in the T_W value would be that the diffusion length L decreases with decreasing water content. The decrease in the diffusion length L can be explained as the decrease in the effective thickness of the diffusion controlled hydrous region with decreasing water content.

Zheng has discussed the drop in specific capacitance of $RuO_2 \cdot xH_2O$ thick films at high scan rate based on proton depletion or oversaturation inside the electrode, which will result in increased ionic resistance and limit the charge/discharge rate and the power

density.[19c] It was suggested that the addition of carbon black acted as a reservoir for electrolyte, rather than acting as an additive to increase the electronic conductivity. The mixing of suitable amounts of carbon black should increase the mass transport through the film by adding additional mesopores. The drop in specific capacitance of $RuO_2 \cdot xH_2O$ thick films at high scan rate is the same phenomenon as the poor capacitor frequency response at high water content observed in this study. On the basis of the electrolyte exhaustion model, the decrease in the effective thickness L for the less hydrated oxides can be interpreted as utilization of active sites deeper into the film.

The decrease in the effective thickness L may also be interpreted as utilization of less-accessible active sites, such as micropores. The electric double-layer capacitance in the mesopores created from anhydrous RuO_2 nanoparticles can be fully utilized.[31] The penetration of ions through the film is restricted to mesopores in the case of anhydrous RuO_2, because of the limited amount of hydrous regions within the primary particle micropores. Mesopores are less influenced by diffusion limitations, giving the high capacitor frequency response with the sacrifice of specific capacitance. The less accessible micropores will be diffusion controlled, and the apparent increase in the effective thickness can be interpreted as the increase in the utilization of hydrated micropores. In the case of $RuO_2 \cdot 0.5H_2O$ at medium frequency, the charge storage arising from the electric double-layer and electrosorption of ions on the surface of nanoparticles originates mainly at mesopores. At low frequency, the ions are able to penetrate through the hydrous region into the micropores. This gives the high specific capacitance due to the larger active surface area and slower frequency response.
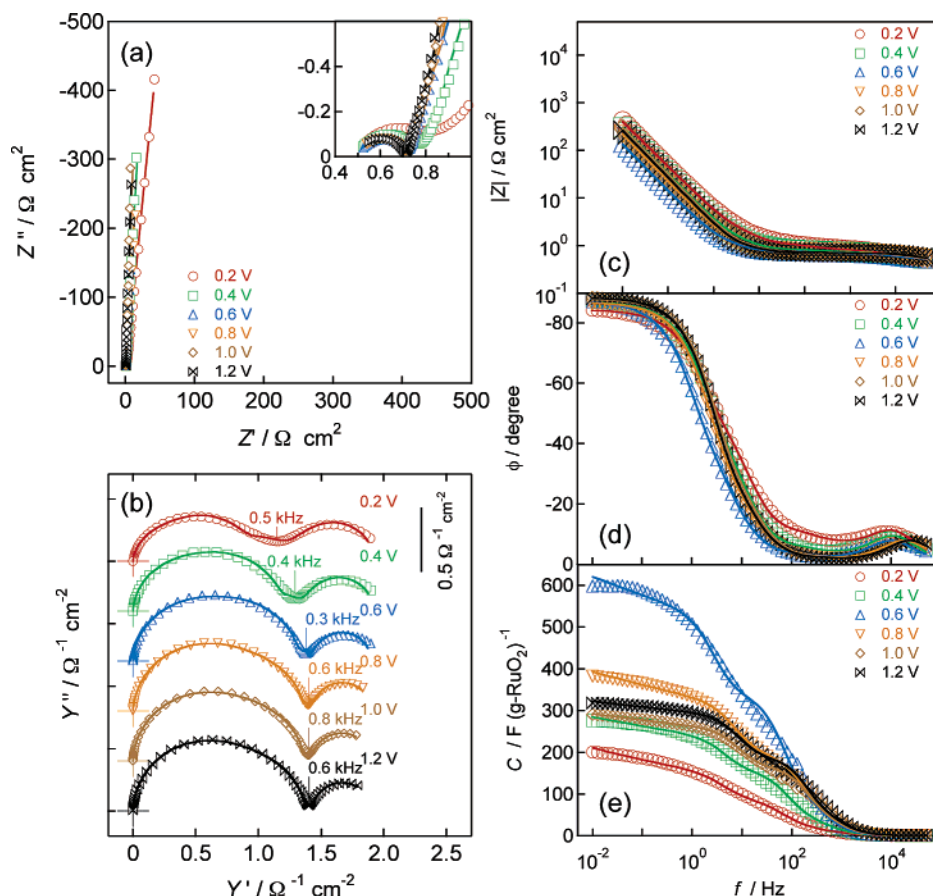
Figure 6. The (a) complex-plane impedance and (b) admittance plots at various electrode potentials for layered $H_{0.2}RuO_{2.1} \cdot nH_2O$. The characteristic knee frequency is shown in b. Frequency dependence of the (c) magnitude $|Z|$, (d) phase angle ϕ, and (e) specific capacitance C. Mass of material: 40 μg. Electrolyte: 0.5 M H_2SO_4 (25 °C). The solid lines represent the fitted data to the equivalent circuit Figure 7.
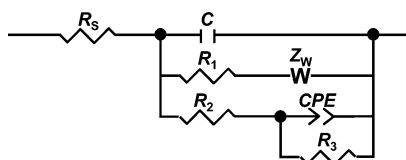
Figure 7. Equivalent circuit for modeling the impedance of $RuO_2 \cdot xH_2O$ and layered $H_{0.2}RuO_{2.1} \cdot nH_2O$.

The strong scan rate dependency observed in the cyclic voltammograms for the intermediate case of $RuO_2 \cdot 0.3H_2O$ supports the above scheme. The redox peaks at ~0.6 V vs RHE in the cyclic voltammograms of $RuO_2 \cdot 0.3H_2O$ are more dependent on the scan rate than $RuO_2 \cdot 0.5H_2O$ or anhydrous RuO_2. The scan rate dependency in $RuO_2 \cdot 0.3H_2O$ was most obvious at potentials where the surface-redox related charge participates. This suggests that in the transitional case between $RuO_2 \cdot 0.5H_2O$ and anhydrous RuO_2, ionic transport through the micropores occurs to some degree, but not as readily as in the case of $RuO_2 \cdot 0.5H_2O$. One must also take into consideration that capacitance from the electric double-layer will also increase if the particle size is smaller.[22b]

A schematic fractal tree-root model is shown in Figure 8 to demonstrate the increase in the diffusion length L according to this model. Primary particles agglomerate into secondary particles forming mesopores, which constitute the thick trunk root. The micropores formed from the primary particles constitute the thin roots. In the mesopores, the effect of mass transfer is insignificant for charging of the electric double-layer since the ionic resistance is low. On the other hand, charging in the micropores is mass transfer controlled since the ionic resistance is high. The primary nanoparticles of $RuO_2 \cdot 0.5H_2O$
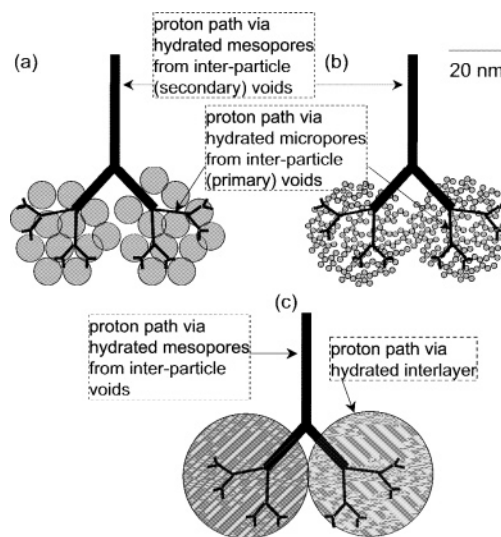
Figure 8. A schematic of the fractal tree-root model for (a) anhydrous RuO_2, (b) hydrous RuO_2, and (c) layered $H_{0.2}RuO_{2.1} \cdot nH_2O$.

are typically less than 2 nm in diameter and are loosely packed, giving appreciable hydrated micropores.[20d] On the contrary, the primary particles of anhydrous RuO_2 are around 10−20 nm in diameter and are densely packed, with almost no micropores.[31] The capacitance in $RuO_2 \cdot 0.5H_2O$ originates from the easily accessible mesopores (thick trunk roots in Figure 8) and the less accessible micropores (thin roots in Figure 8). Although the mesopores are quickly charged, the micropores suffer from mass transfer. The utilization of micropores results in high specific capacitance but gives low capacitor frequency response.

Impedance of Mixed Conducting Hydrous Ruthenates

J. Phys. Chem. B, Vol. 109, No. 15, 2005 **7337**

On the other hand, the majority of the capacitance in anhydrous RuO_2 originates from the easily accessible mesopores (thick trunk roots in Figure 8). Thereby, the capacitor frequency response is high but the specific capacitance is low because of the low surface utilization.

A similar scheme can be drawn for layered $H_{0.2}RuO_{2.1}\cdot nH_2O$ (Figure 8c). In the case of layered $H_{0.2}RuO_{2.1}\cdot nH_2O$, the easily accessible mesopores (thick trunk roots in Figure 8c) are constructed from the interparticle mesoporous voids. The less accessible region (thin roots in Figure 8c) originates from the expandable hydrous interlayer. The W_T parameter for layered $H_{0.2}RuO_{2.1}\cdot nH_2O$ was comparable to that of $RuO_2\cdot 0.3H_2O$, suggesting that the protonic conductivity of the interlayer is comparable to that of the compact, hydrous interparticle micropores of $RuO_2\cdot 0.5H_2O$.

The charge-transfer resistance of $RuO_2\cdot xH_2O$ and layered $H_{0.2}RuO_{2.1}\cdot nH_2O$ was not significantly different. Also, the electronic conduction of these materials are in the same order.[18,26] Such data suggests that the ionic transport most likely dominates the capacitor frequency response. This is attributed to the fact that a large part of the specific capacitance in layered $H_{0.2}RuO_{2.1}\cdot nH_2O$ is achieved within the hydrous interlayer.

5. Conclusions

The protonic and electronic conduction of a series of nanoparticulate ruthenium oxides with different water content, $RuO_2\cdot xH_2O$ (x = 0.5, 0.3, 0), and a layered ruthenic acid hydrate ($H_{0.2}RuO_{2.1}\cdot nH_2O$), was studied by electrochemical impedance spectroscopy and cyclic voltammetry. The knee frequency in the complex-plane plots was independent of the potential and the water content in $RuO_2\cdot xH_2O$. This indicates that the charge-transfer resistance through the film is comparable, and the electronic conduction arising from the difference in the water content in $RuO_2\cdot xH_2O$ does not essentially affect the capacitive behavior. The capacitor response frequency shifted to higher frequency with the decrease in the water content in $RuO_2\cdot xH_2O$. A drastic decrease in the finite length Warburg impedance term T_W in the medium-frequency region was observed with decreasing water content in $RuO_2\cdot xH_2O$. These results show that the capacitor frequency response is dominated by the protonic conduction. The modest capacitor frequency response of $RuO_2\cdot xH_2O$ with high water content and layered $H_{0.2}RuO_{2.1}\cdot nH_2O$ is most likely due to electrolyte exhaustion within the film and/or lower protonic conduction in the hydrous micropores or interlayer. The present results corroborate the importance of hydrous regions (either interparticle or interlayer) to allow substantial protonic conduction in $RuO_2\cdot xH_2O$ and layered $H_{0.2}RuO_{2.1}\cdot nH_2O$ as electrode materials for electrochemical capacitors. The detailed understanding of the charge storage mechanism in these electronic−protonic conducting hydrous materials furnishes new guiding principles into material design for electrochemical capacitor materials intended for high energy and high power applications.

Supporting Information Available: Additional experimental details. This material is available free of charge via the Internet at http://pubs.acs.org.

References and Notes

(1) Conway, B. E. *Electrochemical Supercapacitors*; Kluwer Academic Pub., Norwell, MA, 1999.

(2) Raistrick, I. E. in *Electrochemistry of Semiconductors and Electronics*; McHardy, J., Ludwig, F., Eds.; Noyes Publications: Norwich, NY, 1992; p 297.

(3) Nishino, A. *J. Power Sources* **1996**, *60*, 137.

(4) Faggioli, E.; Rena, P.; Danel, V.; Andriu, X.; Mallant, R.; Kahlen, H. *J. Power Sources* **1999**, *84*, 261.

(5) Burke, A. *J. Power Sources* **2000**, *91*, 37.

(6) Conway, B. E. *J. Electrochem. Soc.* **1991**, *138*, 1539.

(7) Trasatti, S. *Electrochim. Acta* **1991**, *36*, 225.

(8) Sarangapani, S.; Tilak, B. V.; Chen, C.-P. *J. Electrochem. Soc.* **1996**, *143*, 3791.

(9) Conway, B. E.; Birss, V.; Wojtowicz, J. *J. Power Sources* **1997**, *66*, 1.

(10) Takasu, Y.; Murakami, Y. *Electrochim. Acta* **2000**, *45*, 4135.

(11) Angelinetta, C.; Trasatti, S.; Atanasoska, L. D.; Atanasoski, R. T. *J. Electroanal. Chem.* **1986**, *214*, 535.

(12) Trasatti, S.; Lodi, G. in *Electrodes of Conducting Metallic Oxides, part B*; Trasatti, S., Ed.; Elsevier: Amsterdam, 1981; Ch. 11.

(13) Trasatti, S. in *Advances in Electrochemical Science and Engineering, vol. 2*; Gerischer, H., Tobias, C. W., Eds.; VCH: Weinheim, 1992; Ch. 1.

(14) Trasatti, S. *Electrochim. Acta*, **2000**, *45*, 2377.

(15) Trasatti, S. *Electrochim. Acta*, **1987**, *32*, 369.

(16) Trasatti, S.; Buzzanca, G. *J. Electroanal. Chem.* **1971**, *29*, Ap 1.

(17) Zheng, J. P.; Jow, T. R. *J. Electrochem. Soc.* **1995**, *142*, L6.

(18) Zheng, J. P.; Cyang, P. J.; Jow, T. R. *J. Electrochem. Soc.* **1995**, *142*, 2699.

(19) (a) Fang, Q. L.; Evans, D. A.; Roberson, S. L.; Zheng, J. P. *J. Electrochem. Soc.* **2001**, *148*, A833. (b) Zheng, J. P.; Huang, C. K. *J. New Mater. Electrochem. Sys.* **2002**, *5*, 41. (c) Zheng, J. P. *Electrochem. Solid-State Lett.* **1999**, *2*, 359. (d) Fu, R.; Ma, Z.; Zheng, J. P. *J. Phys. Chem. B* **2002**, *106*, 3592. (e) Zheng, J. P.; Jow, T. R. *J. Power Sources* **1996**, *62*, 155. (f) Jow, T. R.; Zheng, J. P. *J. Electrochem. Soc.* **1998**, *145*, 49. (g) Zheng, J. P.; Xin, Y. *J. Power Sources* **2002**, *110*, 86.

(20) (a) Long, J. W.; Swinder, K. E.; Merzbacher, C. I.; Rolison, D. R. *Langmuir* **1999**, *15*, 780. (b) Long, J. W.; Swinder, K. E.; Merzbacher, C. I.; Rolison, D. R. *Langmuir* **2003**, *19*, 2532. (c) Long, J. W.; Ayers, K. E.; Rolison, D. R. *J. Electroanal. Chem.* **2002**, *522*, 58. (d) Dmowski, W.; Egami, T.; Swinder-Lyons, K. E.; Love, C. T.; Rolison, D. R. *J. Phys. Chem. B* **2002**, *106*, 12677. (e) McKeown, D. A.; Hagans, P. L.; Carette, L. P. P.; Russell, A. E.; Swinder, K. E.; Rolison, D. R. *J. Phys. Chem. B* **1999**, *103*, 4825.

(21) For example; (a) Vukovic, M.; Cukman, D. *J. Electroanal. Chem.* **1999**, *474*, 167. (b) Hu, C.-C.; Huang, Y.-H. *J. Electrochem. Soc.* **1999**, *146*, 2465. (c) Kim, I.-H.; Kim, K.-B. *Electrochem. Solid-State Lett.* **2001**, *4*, A62.

(22) (a) Miller, J. M.; Dunn, B.; Tran, T. D.; Pekala, R. W. *J. Electrochem. Soc.* **1997**, *144*, L309. (b) Takasu, Y.; Matsuo, C.; Ohnuma, T.; Ueno, M.; Murakami, Y. *Chem. Lett.* **1998**, *1998*, 1235. (c) Miller, J. M.; Dunn, B. *Langmuir* **1999**, *15*, 799. (d) Lin, C.; Ritter, J. A.; Popov, B. N. *J. Electrochem. Soc.* **1999**, *146*, 3155. (e) Sato, Y.; Yomogida, K.; Nanaumi, T.; Kobayakawa, K.; Ohsawa, Y.; Kawai, M. *Electrochem. Solid-State Lett.* **2000**, *3*, 113. (f) Zhang, J.; Jiang, D.; Chen, B.; Zhu, J.; Jiang, L.; Fang, H. *J. Electrochem. Soc.* **2001**, *148*, A1362. (g) Ramani, M.; Haran, B. S.; White, R. E.; Popov, B. N. *J. Electrochem. Soc.* **2001**, *148*, A374. (h) Nanaumi, T.; Ohsawa, Y.; Kobayakawa, K.; Sato, Y. *Electrochemistry* **2002**, *70*, 681.

(23) (a) Ma, R.; Wei, B.; Xu, C.; Liang, J.; Wu, D. *Bull. Chem. Soc. Jpn.* **2000**, *73*, 1813. (b) Iwata, T.; Hirose, T.; Ueda, A.; Sawatari, N. *Electrochemistry* **2001**, *69*, 177. (c) Kim, H.; Popov, B. N. *J. Power Sources* **2002**, *104*, 52. (d) Hu, C.-C.; Wang, C.-C. *Electrochem. Commun.* **2002**, *4*, 554. (e) Park, J. H.; Ko, J. M.; Park, O. O. *J. Electrochem. Soc.* **2003**, *150*, A864. (f) Machida, K.; Furuuchi, K.; Min, M.; Naoi, K. *Electrochemistry* **2004**, *72*, 402. (g) Hu, C.-C.; Chen, W.-C.; Chang, K.-H. *J. Electrochem. Soc.* **2004**, *151*, A281. (h) Qin, X.; Durbach, S.; Wu, G. T. *Carbon* **2004**, *42*, 423.

(24) Sugimoto, W.; Iwata, H.; Yasunaga, Y.; Murakami, Y.; Takasu, Y. *Angew. Chem., Int. Ed.* **2003**, *42*, 4092.

(25) Sugimoto, W.; Iwata, H.; Murakami, Y.; Takasu, Y. *J. Electrochem. Soc.* **2004**, *151*, A1181.

(26) Sugimoto, W.; Omoto, M.; Yokoshima, K.; Murakami, Y.; Takasu, Y. *J. Solid State Chem.* **2004**, *177*, 4542.

(27) For example; (a) Rishpon, J.; Gottesfeld, S. *J. Electrochem. Soc.* **1984**, *131*, 1960. (b) Da Silva, L. A.; Alves, V. A.; Da Silva, M. A. P.; Trasatti, S.; Boodts, J. F. C. *Can. J. Chem.* **1997**, *75*, 1483. (c) Vallet, C. E.; Tilak, B. V.; Zuhr, R. A.; Chen, C.-P. *J. Electrochem. Soc.* **1997**, *144*, 1289. (d) Suleimanov, A. S. *Electrokim.* **1989**, *25*, 632. (e) Chen, L.; Guay, D.; Lasia, A. *J. Electrochem. Soc.* **1996**, *143*, 3576. (f) Horvat-Radosevic, V.; Kvastek, K.; Vukovic, M.; Cukman, D. *J. Electroanal. Chem.* **2000**,

482, 188. (g) Tilak, B. V.; Birss, V. I.; Wang, J.; Chen, C.-P.; Rangarajan, S. K. *J. Electrochem. Soc.* **2001**, *148*, D112. (h) Hughes, M.; Shaffer, M. S.; Renouf, A. C.; Sing, C.; Chen, G. Z.; Fray, D. J.; Windle, A. H. *Ad. Mater.* **2002**, *14*, 382. (i) Doubova, L. M.; Daolio, S.; De Battisti, A. *J. Electroanal. Chem.* **2002**, *532*, 25. (j) Nian, Y.-R.; Teng, H. *J. Electrochem. Soc.* **2002**, *149*, A1008. (k) Hughes, M.; Chen, G. Z.; Shaffer, M. S. P.; Fray, D. J.; Windle, A. H. *Chem. Mater* **2002**, *14*, 1610. (l) Santana, M. H. P.; Da Silva, L. M.; De Daria, L. A. *Electrochim. Acta* **2003**, *48*, 1885. (m) Liu, X. M.; Zhang, X. G. *Electrochim. Acta* **2004**, *49*, 229. (n) Mohamedi, M.; Yamashina, M.; Uchida, I.; Umeda, M. *Electrochemistry* **2004**, *1*, 14.

(28) For example; (a) Fiordiponti, P.; Pistoia, G. *Electrochim. Acta* **1989**, *34*, 215. (b) Srinivasan, V.; Weidner, J. W. *J. Electrochem. Soc.* **1999**, *146*, 1650. (c) Fusalba, F.; El Mehdi, N.; Breau, L.; Bélanger, D. *Chem. Mater.* **1999**, *11*, 2743. (d) Talbi, H.; Just, P.-E.; Dao, L. H. *J. Appl. Electrochem.* **2003**, *33*, 465. (e) Lufrano, F.; Staiti, P.; Minutoli, M. *J. Power Sources* **2003**, *124*, 314. (f) Kierzek, K.; Frackowiak, E.; Lota, G.; Gryglewicz, G.; Machnikowski, J. *Electrochim. Acta* **2004**, *49*, 515. (g) Hasbach, A.; Retter, U.; Siegler, K.; Kautek, W. *J. Electroanal. Chem.* **2004**, *561*, 29.

(29) Schmidt, T. J.; Noeske, M.; Gasteiger, H. A.; Behm, R. J.; Britz, P.; Bönnemann, H. *J. Electrochem. Soc.* **1998**, *145*, 925.

(30) Schmidt, T. J.; Gasteiger, H. A.; Stäb, G. D.; Urban, P. M.; Kolb, D. M.; Behm, R. J. *J. Electrochem. Soc.* **1998**, *145*, 2354.

(31) Sugimoto, W.; Kizaki, T.; Yokoshima, K.; Murakami, Y.; Takasu, Y. *Electrochim. Acta* **2004**, *49*, 313.

(32) Doblhofer, K.; Metikos, M.; Ogumi, Z.; Gerischer, H. *Ber. Bunsen-Ges. Phys. Chem.* **1978**, *82*, 1046.

(33) The value of n cannot be defined in the aqueous state. The average n value is typically $n \sim 0.9$ for a room-temperature dried product and $n \sim 0$ after drying at 120 °C overnight. XRD reveals that the room-temperature dried product may be composed of a mixture of mono-, di-, and trihydrated phases (see ref 25).

(34) (a) Ho, C.; Raistrick, I. D.; Huggins, R. A. *J. Electrochem. Soc.* **1980**, *127*, 343. (b) Hunter, T. B.; Tyler, P. S.; Smyrl, W. H.; White, H. S. *J. Electrochem. Soc.* **1987**, *134*, 2198. (c) Penner, R. M.; Martin, C. R. *J. Phys. Chem.* **1989**, *93*, 984. (d) Amemiya, T.; Hashimoto, K.; Fujishima, A. *Denki Kagaku (presently Electrochemistry)* **1992**, *60*, 1075. (e) Amemiya, T.; Hashimoto, K.; Fujishima, A. *J. Phys. Chem.* **1993**, *97*, 4187. (f) Amemiya, T.; Hashimoto, K.; Fujishima, A. *J. Phys. Chem.* **1993**, *97*, 4192. (g) Amemiya, T.; Hashimoto, K.; Fujishima, A. *J. Phys. Chem.* **1993**, *97*, 9736. (h) Kim, J. J.; Amemiya, T.; Tryk, D. A.; Hashimoto, K.; Fujishima, A. *J. Electroanal. Chem.* **1996**, *416*, 113. (i) Kim, J. J.; Tryk, D. A.; Amemiya, T.; Hashimoto, K.; Fujishima, A. *J. Electroanal. Chem.* **1997**, *435*, 31. (j) Hong, J.-i.; Yeo, I.-H.; Paik, W.k. *J. Electrochem. Soc.* **2001**, *148*, A156.